Energy Storage Materials 14 (2018) 230–237

Contents lists available at ScienceDirect

Energy Storage Materials

journal homepage: www.elsevier.com/locate/ensm

Magnetically enhanced plasma exfoliation of polyaniline-modified graphene for flexible solid-state supercapacitors

Keliang Wang*, Bocong Zheng, Maheshwar Shrestha, Thomas Schuelke, Qi-Hua Fan*

Department of Electrical Engineering and Computer Engineering & Department of Chemical Engineering and Materials Science, Michigan State University, East Lansing, MI 48824, United States

ARTICLE INFO

Keywords:
Plasma
Graphene
Flexible
Solid-state
Supercapacitor

ABSTRACT

Flexible solid-state supercapacitors featuring lightweight and large capacitance have many attractive applications in portable and wearable electronics. Nitrogen-doped graphene is a promising electrodes material due to the extraordinary properties of graphene. This study demonstrates a magnetically enhanced dielectric barrier discharge that has the potential to efficiently exfoliate polyaniline-modified graphene at low input power. The plasma exfoliated N-doped graphene is subsequently used to fabricate flexible solid-state supercapacitors, which exhibit large specific capacitance of 45 mF/cm^2 at 0.2 A cm^{-2} charging rate, ~100% capacitance retention after 1000 charge/discharge cycles at different current densities, and outstanding mechanical flexibility. The magnetically enhanced plasma exfoliation of graphite oxide offers a potentially cost-effective approach to producing high-quality carbon nanomaterials for energy storage.

1. Introduction

Portable and wearable electronics, such as smart watches, bendable displays, wearable sensors, artificial electronic skin, and implantable medical devices, have been explosively increasing in recent years. Flexible batteries and supercapacitors are the essential components in these devices [1–4]. Among the energy storage components, flexible supercapacitors exhibit attractive features, such as fast charge/discharge rates, high power density, and long operation life. Similar to conventional supercapacitors, flexible supercapacitors include symmetric and asymmetric flexible supercapacitors. The symmetrical supercapacitors present more stable performance because they use carbon-based electrode materials that can withstand the harsh electrolytes.

Carbon nanotubes, carbon fibers, and activated carbon have been extensively studied as the electrode materials in symmetric supercapacitors [5–7]. However, only limited capacitances of ~20% of the theoretical values were achieved [8]. Recently, it was found that polypyrrole, polyaniline and polythiophene [7,9,10] could improve the capacitance performance of carbon electrodes *via* a pseudocapacitive effect arose from the nitrogen element contained in these polymers [11–16]. On the other hand, graphene has been considered an excellent energy storage material owing to its outstanding mechanical strength, high electrical conductivity, large specific surface area, giant electron mobility, and high theoretical capacitance [17,18]. So far, a variety of methods have been developed to fabricate graphene, including mechanical cleaving, epitaxial growth, chemical vapor deposition, tearing of carbon nanotubes, reduction of graphene oxide, and direct exfoliation of graphite [19–22]. Nevertheless, most of the methods involve high-temperature processes under high vacuum and are energy intensive with complex procedures.

Recently, plasma etching technology was reported in the preparation of highly efficient electrocatalysts for oxygen evolution reaction and water oxidation [23–26]. Meanwhile, a recent study indicated that graphite oxide (GO) could be rapidly exfoliated into graphene at room temperature by plasmas and supercapacitors made of CH_4 plasma exfoliated graphene displayed excellent capacitance performance [27]. Based on the optical emission spectroscopy analysis, the efficiency of GO exfoliation depended on the plasma density [27]. This effect could be understood from two aspects: 1) a higher plasma density leads to more negatively charged GO surfaces due to fast electron accumulation; and 2) a higher density plasma contains more reactive species (e.g. H^+ ions) that break the C-O-C bonds. In typical discharges, the plasma densities are proportional to the applied power and the loss of high-energy electrons accounts for an essential reason of limited plasma density. Therefore, reducing the loss of high-energy electrons and achieving high plasma density with low input power are expected to enable energy-efficient exfoliation of GO and subsequent low-cost energy storage devices.

This study aims to develop efficient plasma exfoliation of GO that can be subsequently used for flexible energy storage devices. The research includes a combined effort of the following three aspects: 1)

* Corresponding authors.
E-mail addresses: klwang@egr.msu.edu (K. Wang), qfan@egr.msu.edu (Q.-H. Fan).

https://doi.org/10.1016/j.ensm.2018.04.004
Received 17 January 2018; Received in revised form 18 March 2018; Accepted 5 April 2018
Available online 07 April 2018

establishing a magnetically enhanced dielectric barrier discharge (MEDBD) through modeling to create high-density plasmas; 2) plasma exfoliation of polyaniline-modified GO to obtain N-doped graphene; and 3) fabricating high-performance solid-state flexible supercapacitors using the plasma-exfoliated N-doped graphene.

2. Experimental and theoretical methods

2.1. Preparation of activated carbon

Graphite oxides were prepared by oxidizing of graphite with a modified Hummers' method. Graphite flakes (2.5 g, Fisher Scientific) were mixed with concentrated sulfuric acid (H_2SO_4, 75 ml, Fisher Scientific) under vigorous stirring at 0 °C for 4 h. Then, sodium nitrate ($NaNO_3$, 1.25 g, Fisher Scientific) and potassium permanganate ($KMnO_4$, 7.5 g, Fisher Scientific) were slowly added in sequence. After 12 h of reaction at room temperature, 25 ml deionized water was slowly added into the mixture and the temperature was increased to 98 °C before additional 75 ml deionized water was added. After 4 h, 7.5 ml hydrogen peroxide (H_2O_2, 30 *wt*% Fisher Scientific) was dropwise added and yellow colloid was formed. Then, the mixture was transferred into a dialysis tubing (14,000 MWCO Daltons, Fisher Scientific) to dialyze in deionized water for 7 days till the pH was close to 7. The dialyzed sample was stored in a refrigerator and denoted in short for GO.

2.2. Preparation of aniline modified GO

Aniline ($C_6H_5NH_2$, 5 ml, Fisher Scientific) was dispersed into 15 mL ethanol, followed by adding 20 g GO colloid in a ball mill jar (100 mL). The mixture was grinded by a planetary ball mill (PMQW0.4 L, Nanjing Chishun Science & Technology Co., Ltd.) at 450 rpm for 30 min. Then, the grinded mixture was transferred into a petri dish (100 × 1 mm, Fisher Scientific) and dried naturally. The dried product was denoted as GO-PANi.

2.3. Preparation of aniline modified graphene

Aniline modified graphene was prepared using a magnetically enhanced dielectric barrier discharge system schematically illustrated in Fig. 1.The system consisted of a quartz container, a vacuum pump, a vacuum gauge, a mass flow controller, two copper electrodes (~2 × 2 cm) attached to the outside surface of the quartz container (inner surface distance: 2.5 cm), a set of magnets that generated a magnetic field of ~1500 Gauss parallel to the electrodes surfaces, and a 13.56 MHz RF power supply with a matching network. Modeling of the discharges and the resulting plasma characteristics will be discussed later. To prepare aniline modified graphene, 200 mg of GO-PANi was placed in the quartz tube in between the electrodes. Then, the system was evacuated down to ~10 mTorr and purged with the process gas (10% methane in Ar) for five times to ensure the residual air in the tube was negligible. After that, the gas pressure was set to ~80 mTorr by adjusting the mass flow controller. Then the RF power was turned on, starting with 20 W input power, and the matching network was tuned to achieve almost zero-watt reflection power. The RF power was then gradually increased to 45 W, at which the GO-PANi was exfoliated. After the exfoliation, the RF power was turned off and the vacuum system was vented to collect the exfoliated sample denoted as r-GO-PANi-CH_4. It was worth noting that exfoliating of GO-PANi in CH_4 plasmas at the same 80 mTorr pressure would require a much higher RF power of 120 W if no magnetic field was applied.

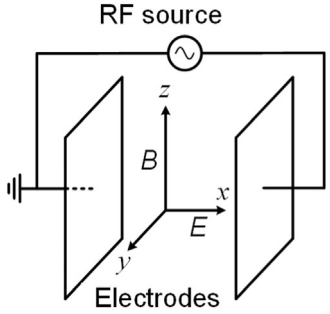

Fig. 1. The schematic diagram of the magnetically enhanced dielectric barrier discharge system used for producing the aniline modified graphene.

2.4. Preparation of flexible supercapacitors

Carbon cloth (MPL Carbon Cloth, Fuel Cell Earth) that served as current collector was cut into 2×1 (length × width) cm^2 pieces and cleaned by alcohol, acetone, and distilled water in turn. After that, slurry of the electrode materials made of r-GO-PANi-CH_4, acetylene black and PTFE with a mass ratio of 8:1:1 was pressed onto the carbon cloth; the carbon electrode area was 1 × 1 (length × width) cm^2. The electrodes were subsequently dried in an oven at 60 °C for 12 h. PVA-H_2SO_4 electrolyte was prepared by mixing 2 g of poly vinyl alcohol (PVA) powder and 2 g concentrated sulfuric acid with 20 mL of DI water. The mixture was subsequently heated to 100 °C under vigorous stirring until the solution became clear. The prepared electrodes were immersed into the gel electrolyte for 10 min and then put into a fume hood for 24 h to allow the electrolyte to cure into solid. Then, two of the electrodes were pressed together with the edges sealed by silicon glue. For convenient measurements, metal wires were connected to the electrodes with conductive silver paste.

2.5. Physical characterization

The microstructures of the samples were characterized by X-ray diffraction (XRD) (Rigaku Smartlab, Rigaku Americas, Inc. USA). The morphologies of the plasma exfoliated graphene were confirmed by transmission electron microscopy (TEM) (JEM-2200FS, JEOL, Japan) at an acceleration voltage of 200 kV. Raman spectra were obtained on a Horiba LABRam confocal Raman system with an excitation wavelength of 532 nm from a diode pumped solid-state laser. X-ray photoelectron spectroscopy (XPS) was performed on an SSX-100 system (Surface Science Laboratories, Inc.) equipped with a monochromated Al K_α X-ray source. An optical spectrometer (FLAME-T-XR1-ES, Ocean Optics, Inc. USA) was used to record the plasma emission spectra.

2.6. Electrochemical characterization

Electrochemical measurements, including cyclic voltammetry (CV) and electrochemical impedance spectroscopy (EIS), were conducted on an Autolab electrochemical work station (PGSTAT128N, Metrohm). The galvanostatic charge/discharge tests were performed on a battery test system (BTS series, NEWARE, China).

2.7. Modeling of magnetically enhanced dielectric barrier discharges

A fluid plasma model was developed to verify the effects of the magnetic field and guide the design of the magnetically enhanced dielectric barrier discharge. The model was equivalent to a parallel plate dielectric barrier discharge. Hence, a one-dimensional model was valid. N_2 gas was used in the model to demonstrate the effects of the magnetic field and avoid unnecessarily complicated chemical reactions in the plasmas. The details of the modeling process are described in S1 section in the Supplementary document.

The above models of plasma discharges with and without a magnetic field were established in a commercial software COMSOL [28]. The species considered in the nitrogen plasmas were electrons, N_2^+, N_2^*, N^+ and N. where N_2^* was an equivalent excited state of N_2

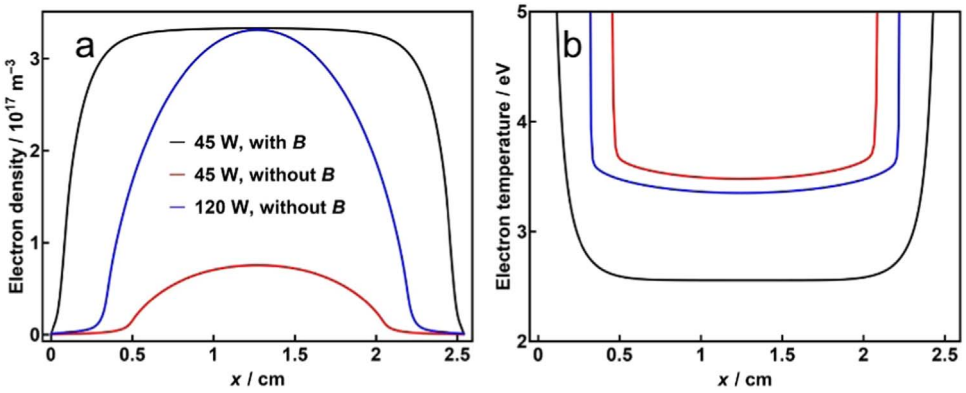

Fig. 2. Time-averaged electron density (a) and electron temperature (b) profiles without/with a magnetic field B under the working pressure of 80 mTorr and the RF power of 45 W, and without the magnetic field B under the RF power of 120 W.

determined from its total cross section for electronic excitation [29]. The rate coefficients used in the model are shown in Table S1. For plasma discharges under relatively high pressures as those used in the exfoliation, the electron energy distribution function (EEDF) was assumed as Maxwellian in the modeling.

3. Results and discussion

Using the one-dimensional plasma model described above, the magnetic enhancement of the dielectric barrier discharges was verified and proven effective. The time-averaged electron density and tempera-

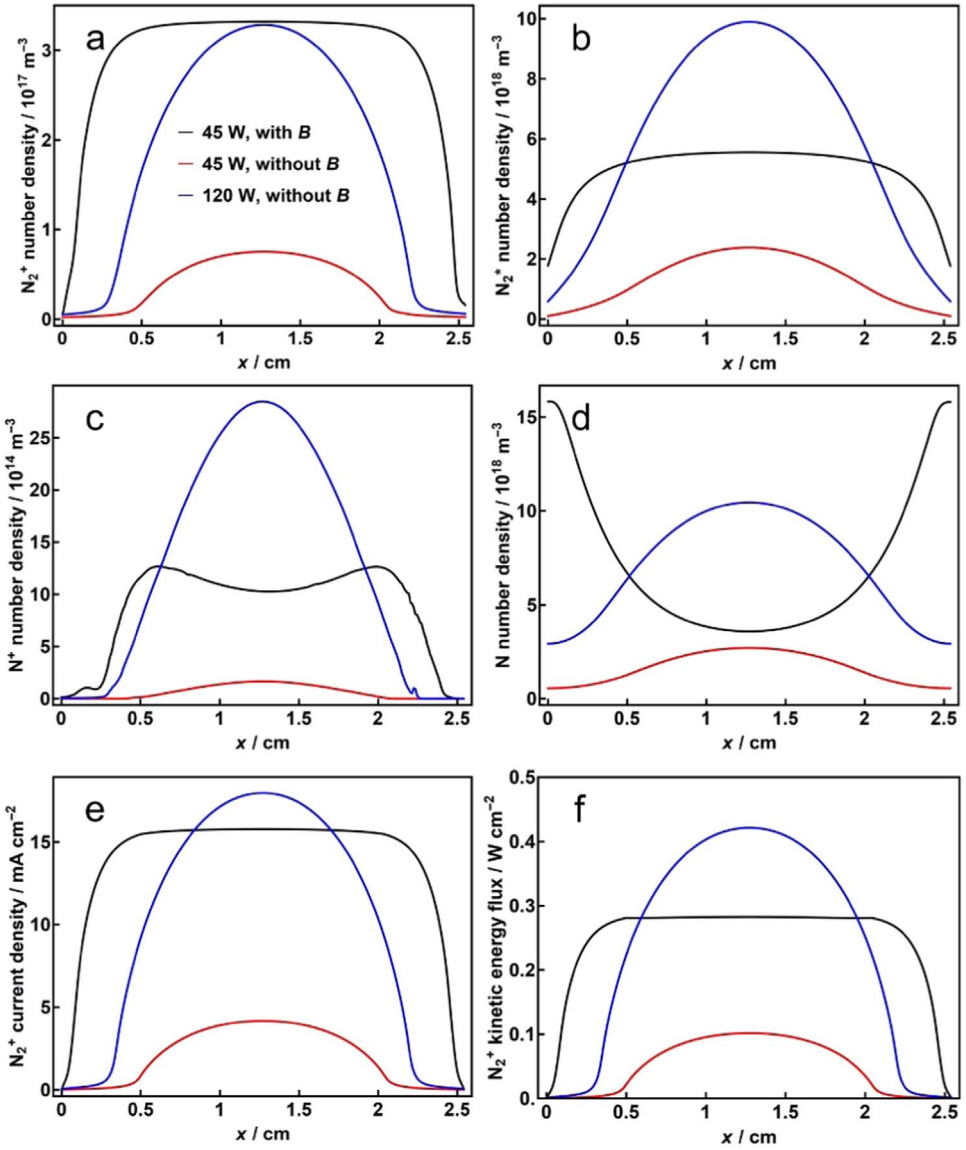

Fig. 3. Number density profiles of N_2^+ (a), N_2^* (b), N^+ (c) and N (d) species, the current density (e) and the kinetic energy flux of N_2^+ (f) under the same conditions as Fig. 2.

ture profiles at different discharge parameters are illustrated in Fig. 2. From Fig. 2**a** it can be seen that under a pressure of 80 mTorr and RF power of 45 W, the maximal electron density increased significantly from around $0.75 \times 10^{17} m^{-3}$ to more than $3 \times 10^{17} m^{-3}$ by applying a strong magnetic field parallel to the electrode surface. This substantial increase in the plasma density was due to the magnetized electrons that were trapped and underwent more collisions with the background gas species, resulting in an increased power coupling efficiency to the plasmas. The sheath thickness was reduced after applying a magnetic field, which had been experimentally observed [30]. The electron density without a magnetic field at a higher RF power of 120 W was demonstrated in Fig. 2**a** as well. The maximal value of about $3.2 \times 10^{17} m^{-3}$ was close to the maximal electron density with a magnetic field at a lower RF power of 45 W. Fig. 2**b** shows that the electron temperatures peak near the electrodes due to the electron heating in the plasma sheath and become flat in the bulk plasma region. The electron temperature without a magnetic field was around 3.5 eV and decreased slightly as increasing the RF power from 45 W to 120 W. By applying the magnetic field, the electron temperature reduced significantly to about 2.5 eV, since the power coupling efficiency as well as the electron-impacted reactions were enhanced.

Fig. 3 demonstrates the number density profiles of various species as well as the N_2^+ ion current density and the kinetic energy flux in the plasma. The N_2^+ number density profiles as shown in Fig. 3**a** are similar to the electron density profiles (Fig. 2**a**). This indicated that the N_2^+ ions were the dominating positively charged species in the plasma. For the excited N_2 species, its number density decreased in the bulk plasma region as the power was reduced as shown in Fig. 3**b**, if no magnetic field was applied. The N^+ species had similar profiles to the N_2^+ species, as shown in Fig. 3**c**. However, the number density was still 2 magnitudes smaller compared with the N_2^+ and therefore could be neglected. The N atoms were mainly generated from the dissociation of N_2 molecules, the dissociation rate decreased significantly at low electron temperatures. As illustrated in Fig. 3**d**, the number density of N atoms at 45 W with a magnetic field peaked near the electrodes and decreased rapidly in the bulk plasma region. However, the number density of N atoms without the magnetic field at 120 W had an opposite tendency. Assuming that the ion flux onto the sample surface was $n_e u_B$ and there was a floating sheath formed around the sample surface with a potential drop of [31] $V_s = -T_e \ln (M_i/2\pi m_e)^{1/2}$, the ion current density and the kinetic energy flux of N_2^+ species can be obtained as $en_e u_B$ and $n_e u_B(V_s + 1/2T_e)$ (where the $1/2T_e$ was the ion energy at the sheath-presheath boundary [31]), as illustrated in Fig. 3**e** and **f**. Since the ion current was proportional to the $T_e^{1/2}$ and the ion kinetic energy flux was proportional to the $T_e^{3/2}$, their maximal values in the bulk plasma region under 120 W without a magnetic field surpassed the maximal values under 45 W with the magnetic field. However, the spatially-averaged ion current density and the ion kinetic energy flux were similar under the above two conditions. Combining the modeling results with the experimental observation that the GO exfoliation occurred at 120 W without a magnetic field and 45 W with a magnetic field, respectively, one could deduce that the ion current density or the ion kinetic flux determined by the electron density and temperature was the control variable in the GO exfoliation process. The other plasma parameters appeared quite different under these two discharge conditions and were unlikely the factor that essentially control the GO exfoliation.

High resolution optical emission spectroscopy (OES) was used to verify the plasma discharge characteristics. Fig. S1 illustrates the plasma emission spectra under 80 mTorr CH_4 pressure at different powers with/without the magnetic field. The intensities of the plasma emissions were 3–4 times higher at different input RF powers when a magnetic field was applied. This observation was quite consistent with the modeling results. Hence, exfoliate GO at low input powers with the assistance of a magnetic field became possible. The same trend was also observed at higher pressure, e.g. 2 Torr, as illustrated in Fig. S2, showing that the intensities of CH_4 plasma emissions increased 2–3 times when a magnetic field was applied.

Fig. 4 shows the optical emission spectra before and right after the plasma exfoliation of GO-PANi in CH_4 gas at 80 mTorr pressure with/without the magnetic field enhancement. The threshold discharge powers of exfoliation were 120 W without the magnetic field and 45 W with the magnetic field. With the plasma density being the primary factor that contributed to the exfoliations, it was clear that the magnetic field led to an increase in the plasma densities. The prominent emission lines included Ar* (690–900 nm), H_α (656.3 nm), H_β (480 nm), C_2 (436–517 nm), and C (193–248 nm), which were observed in all the spectra [32–35], while OH (306.7–308.9 nm) [35] and O_2* lines (480–580 nm) appeared after the exfoliation. These results confirmed that the exfoliations were due to the breakage of the C-O-C bonds; the recombination of O atoms formed O_2 molecules and the subsequent thermal expansion of the O_2 in the plasmas created graphene and/or graphite nano-sheets [27]. It was worth noting that the emission intensities from the newly generated species after the exfoliations with and without the magnetic field were similar, which indicated that the extents of the C-O-C bond breakage were at the same magnitude in the two exfoliation conditions. The lower emission intensity at 120 W without the magnetic field enhancement before the plasma exfoliation could be attributed to the gas rarefaction effect, since the gas number density under a given pressure was reduced at higher gas temperature, which was caused by the higher RF power input. The immediate benefits of the magnetically enhanced plasma exfoliation were lower power and less reactive gas consumptions.

Fig. S3 showed the digital photographs of the graphite oxides before and after CH_4 plasma exfoliation. The morphology apparently changed from a piece of membrane into loose powder, which was potentially graphene. XRD measurement was performed to confirm the materials microstructures (Fig. 5**a**). A sharp peak located at a 2θ angle of ~8.4° was observed for the GO sample, corresponding to a *d*-spacing of 1.05 nm, which was attributed to the (002) planes in the graphite flasks that accommodated oxygen groups and water molecules after the oxidation treatment [36]. In addition, a broad peak with low-intensity located at ~17° was also observed, which might arise from the inhomogeneous structures in GO [37]. On the other hand, the sharp peak completely disappeared after the CH_4 plasma exfoliation and a broad peak centered at 2θ = 23.8° appeared, corresponding to

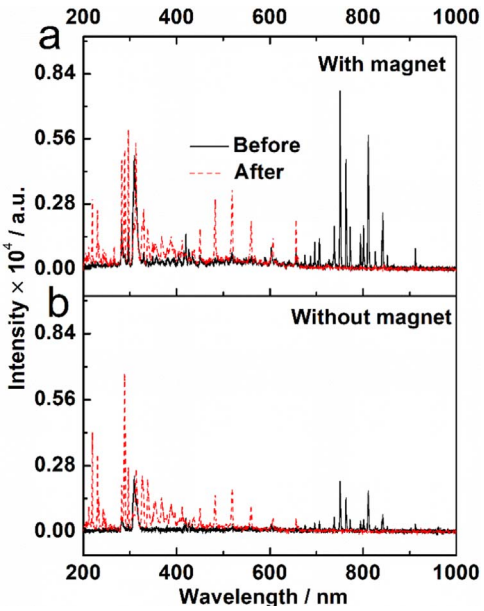

Fig. 4. Optical emission spectra before and after the CH_4 plasma exfoliation of the GO-PANi. (a) With the magnetic field at 45 W RF power, and (b) without the magnetic field at 120 W RF power.

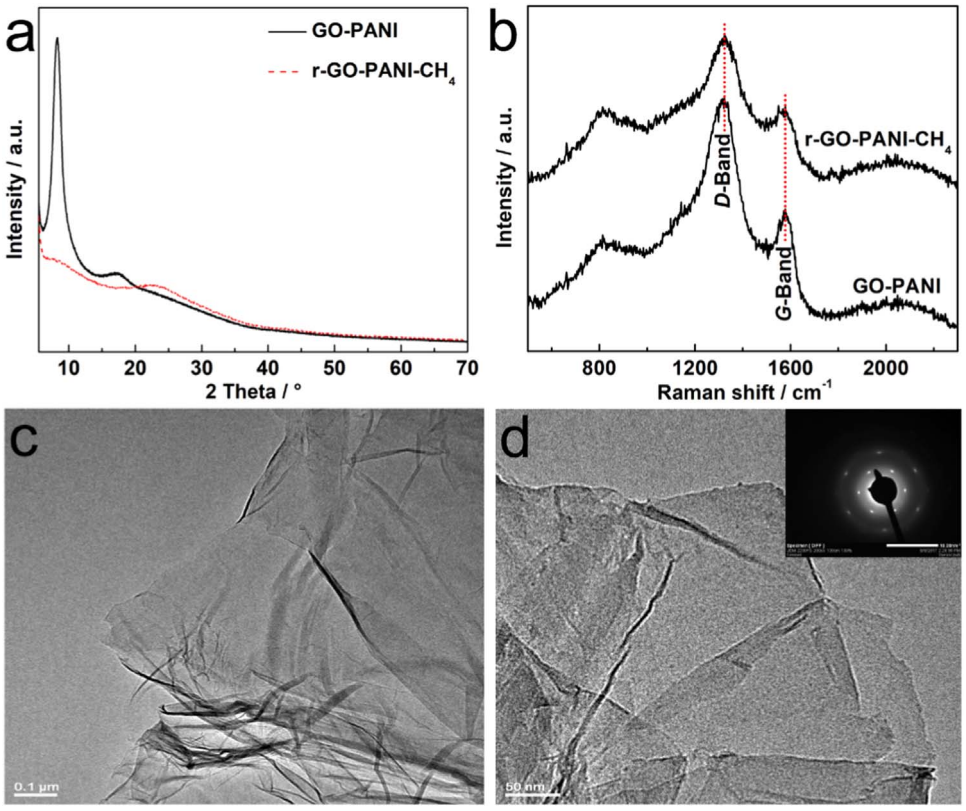

Fig. 5. XRD patterns (a), Raman spectra of GO-PANi and (b), and different magnifications TEM images of r-GO-PANi-CH_4 (c, d).

graphene sheets with a *d*-spacing of 0.37 nm. The dramatically decreased *d*-spacing indicated that the oxygen-containing species in the GO interlayers were removed and the GO was mostly reduced to graphene [36,38].

Fig. 5**b** shows the Raman spectra of the GO and the exfoliated GO (r-GO-PANi-CH_4), respectively. The two characteristic peaks of *D*-band (~1327 cm) and *G*-band were associated with the breathing mode of the rings or *K*-point phonons of A_{1g} symmetry and the E_{2g} vibrational mode present in the sp^2 bonded graphitic carbon, respectively [39,40].

TEM measurements were conducted to confirm the morphologies of the plasma exfoliated materials (Fig. 5**c** and **d**). Typical transparent voile-like structures of graphene were observed, which consisted of crumpled sheets closely associated with each other and formed a disordered regions. Selected-area-electron diffraction (SAED) showed typical hexagonal patterned bright dots (inset in Fig. 5**d**), indicating the presence of graphene sheets in the selected region [41]. Also element mapping was performed to confirm the presence of N (Fig. S4). Apart from the expected primary element C, O and N were also detected. This result suggested that N originated from the aniline was successfully incorporated in the exfoliated powder. In summary of the results of XRD, Raman spectroscopy, TEM, SAED and element mapping, it was clearly demonstrated that N-doped graphene (r-GO-PANi-CH_4) was successfully produced *via* the magnetically enhanced dielectric barrier discharges in CH_4 plasmas.

High resolution XPS was performed (Fig. 6) to obtain further information on the elemental composition and nitrogen bonding configurations in the plasma exfoliated graphene (PANi-CH_4). The XPS survey spectrum was shown in Fig. 6**a**. C, O and N were detected, which was consistent with the results of element mapping. Deconvoluting the high-resolution C 1s spectrum (Fig. 6**b**) indicated the presence of several carbon-containing functional groups: C-C (284.7 eV), C-C/C-N/C-O (285.3 eV), C=O/C=N (286.4 eV) and O=C-O (287.9 eV), which were assigned to sp^2 hybridized carbon, carbon atoms single bonded to carbon, nitrogen or oxygen, carbonyl or amide groups, and ester or carboxylic groups, respectively [42,43]. In O 1s scan (Fig. 6**c**), two types of oxygen-containing groups were verified, including C=O and O=C-O, corresponding to the peaks at 531.2 and 533.5 eV, respectively [42]. In terms of N 1s spectrum (Fig. 6**d**), three peaks with binding energies of 399.4, 400.1 and 401.1 eV were identified, which represented imine nitrogen (-N=), amine nitrogen (-NH-) and positively charged nitrogen (N^+), respectively [44,45]. These functional groups had proven effects in improving the electrical conductivity and electrolyte wettability, and inducing a pseudo capacitance that could greatly improve the capacity of supercapcitors [46–48].

Flexible solid-state supercapacitors with the PVA-H_2SO_4 electrolyte were fabricated using the plasma exfoliated graphene as the electrode materials. The electrochemical characteristics of the assembled supercapacitors were evaluated by CV, EIS, and charge/discharge techniques in a two-electrode configuration. Fig. 7**a** shows the CV results at different scanning rates ranging from 10 to 200 mV s^{-1}. The CV curves exhibited typical rectangular shapes at different scanning rates, indicating good electrical-double-layer-capacitance (EDLC) behavior and electrochemical reversibility. The specific capacitances of the devices were evaluated from the CV curves using the following equation [49]:

$$C_A = \frac{Q}{\Delta V \times S} \quad (1)$$

where C_A (F cm^{-2}) is the areal specific capacitance, Q (C) is the average charge during the charging and discharging process, ΔV (V) is the potential window and S (cm^2) is the area of a r-GO-PANi-CH_4 electrode. The calculated areal specific capacitance were 72, 71, 62, 56 and 48 mF cm^{-2} at the scanning rates of 10, 20, 50, 100 and 200 mV s^{-1}, respectively, which preserved ~67% of the capacitance even at a high scanning rate of 200 mV s^{-1}. These performances were comparable or superior to the previously reported symmetric supercapacitors that used nitrogen-doped carbon materials as the electrodes (see Table S2 for comparison).

Near-linear symmetric triangle curves were observed in the galva-

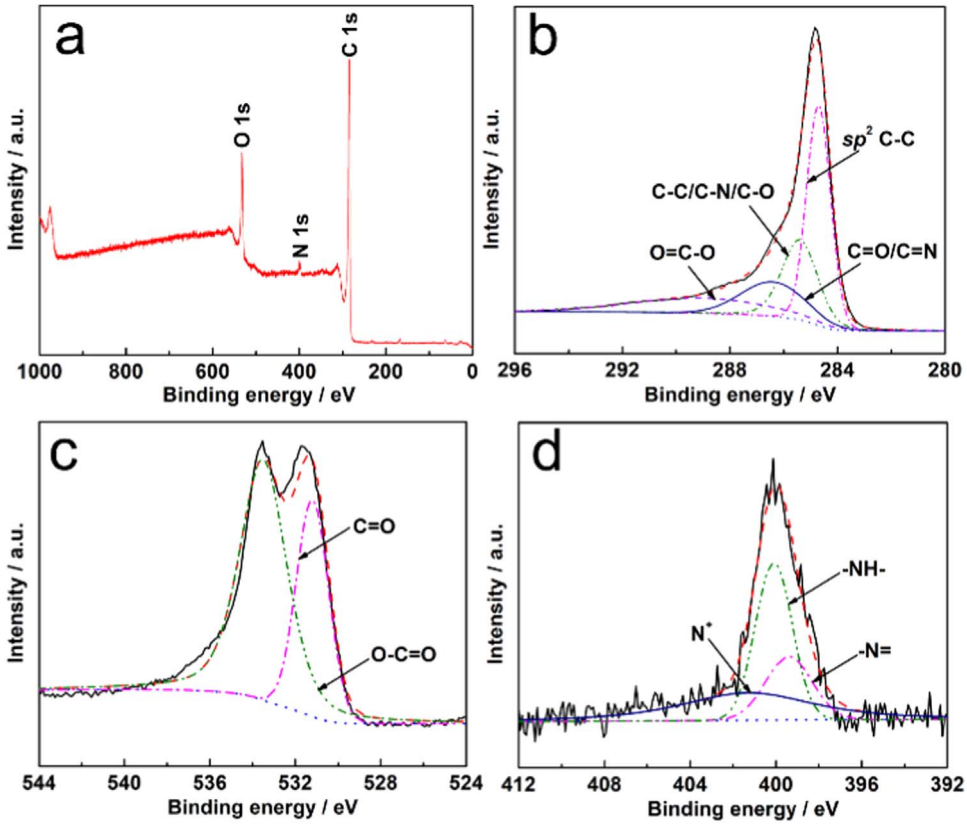

Fig. 6. XPS survey (a) and high-resolution C 1s (b), O 1s (c), and N 1s (d) XPS spectra of r-GO-PANi-CH_4.

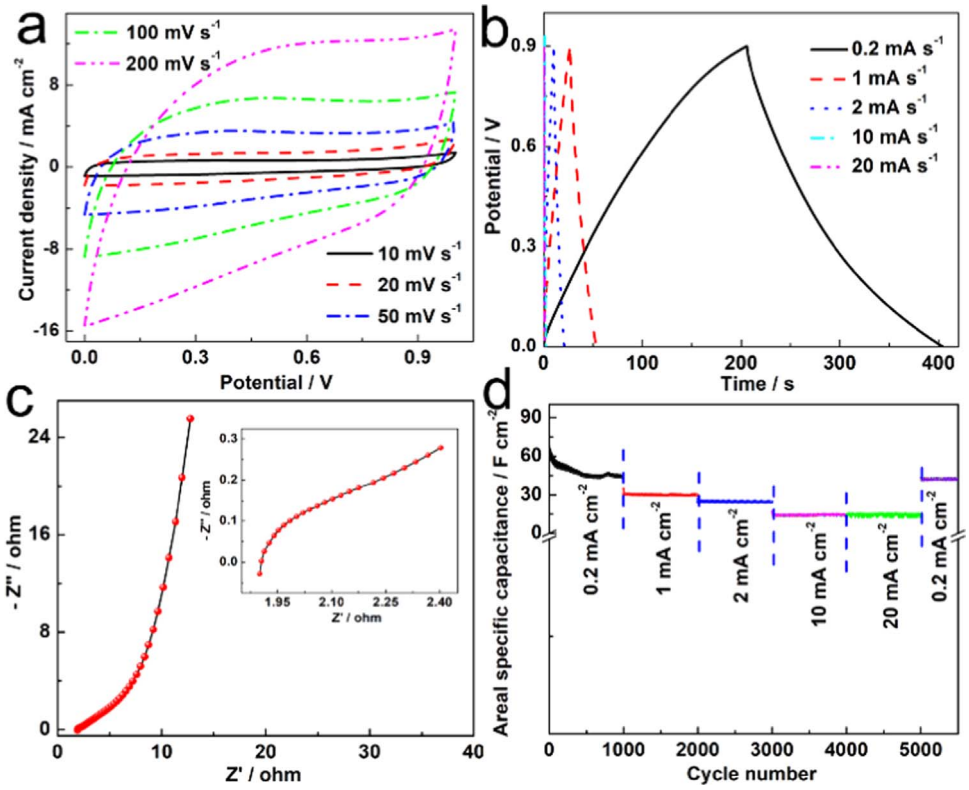

Fig. 7. CV curves (a) at various scanning rates ranging from 10 to 200 mV s^{-1}, galvanostatic charge/discharge curves (b), Nyquist plots (c) and cycle life plot (d) at different current density ranging from 0.2 to 20 mA g^{-1} of r-GO-PANi-CH_4 electrodes, respectively.

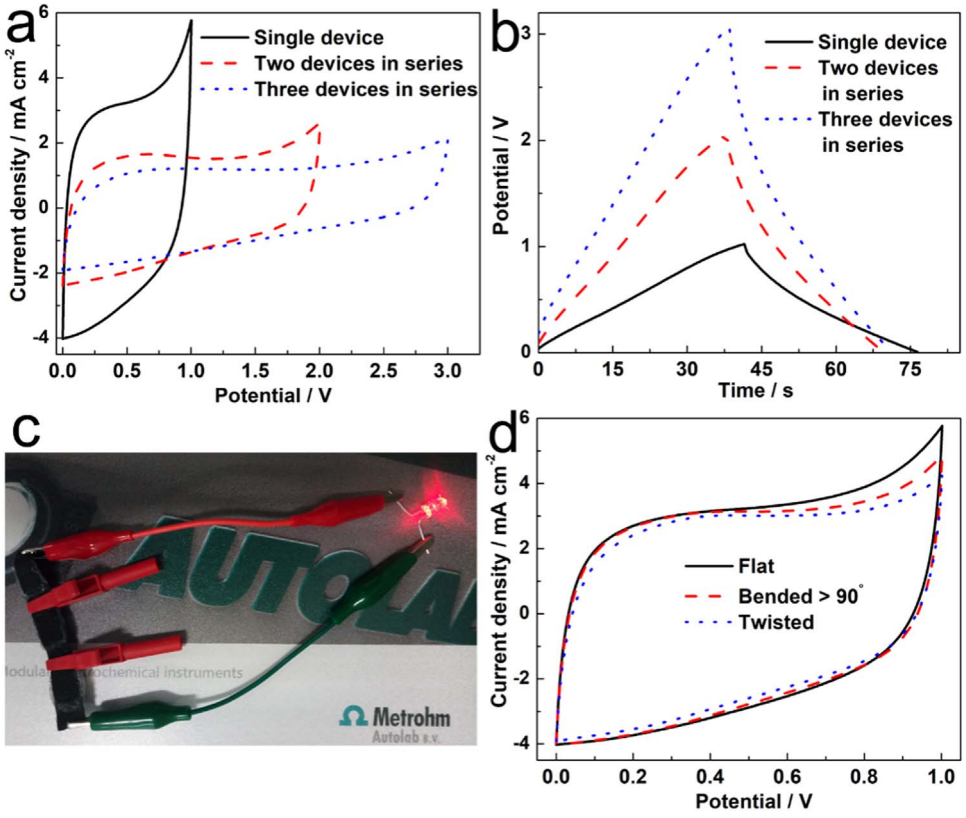

Fig. 8. CV (a) and galvanostatic charge/discharge curves (b) of one, two and three devices in series; Digital photography (c) of powered red LED by three devices connected in series; CV curves (d) of supercapacitor under different deformation.

nostatic charge/discharge measurements of the r-GO-PANi-CH_4 based supercapacitors at different current densities (Fig. 7**b**). This result indicated an excellent reversibility and EDLCs behavior. Additionally, as shown in the Nyquist plots in Fig. 7**c**, electrochemical impedance spectroscopy (EIS) was conducted in a frequency range of 10 mHz to 100 kHz to investigate the ion-transport behavior and electrical resistance. The Nyquist plots consisted of an intercept in real axis in the high-frequency region, an extremely small semicircle in the high and medium frequency regions and a spike line in the low-frequency region, corresponding to low internal resistance (R_s or *ESR,* 1.9 Ω) and low charge transfer resistance at the electrode/electrolyte interface (0.5 Ω), and ideal double-layer charge/discharge behaviors (10.4 Ω) [50,51]. The results confirmed that the plasma exfoliated graphene led to excellent electrical conductivity.

Long-term cycling stability of the assembled devices was tested for 5500 charge/discharge cycles at different current densities. As shown in Fig. 7**d**, the areal specific capacitance declined a little after the initial 1000 cycles at a current density of 0.2 mA cm^{-2}, which might be caused by electro-activation [52]. The capacitance decreased slightly with the increase of the charging current density from 1 to 20 mA cm^{-2}. However, the capacitance retention remained almost 100% in every 1000 cycles at each current density. It was worth noting that, after 5000 cycles, the capacitance at a current density of 0.2 mA cm^{-2} recovered to 41 mF cm^{-2}, which was almost the same as that in the initial scans (45 mF cm^{-2}). These results indicated that the plasma exfoliated graphene electrodes possessed excellent cycling stability and extraordinary reversibility at both low and high charge/discharge current densities.

As a demonstration of the potential applications in flexible electronic devices, two and three of the supercapacitors were connected in series. Fig. 8**a** shows that the voltage windows were two-fold (0–2 V) and three-fold (0–3 V) larger than that of a signal device (0–1 V). Furthermore, typical rectangular shape CV curves at 50 mV s^{-1} were observed, indicating robust and consistent performances of the connected devices. In addition, symmetrical triangle charge/discharge curves were obtained for two and three series-connected devices at a current density of 2 mA cm^{-2} (Fig. 8**b**), further suggesting the ideal capacitance behaviors. The three supercapacitors connected in series were charged to 3 V for 10 s and then used to light up an LED for over 10 min, which demonstrated the promising potential as energy storage devices (Fig. 8**c**). Flexibility tests were conducted upon mechanical deformations. As shown in Fig. 8**d**, CV measurements at 50 mV s^{-1} were performed with the supercapacitor assembly being bent (> 90°) and twisted. The CV curves nearly did not show any distortion, which proved the superior mechanical flexibility and electrochemical stability of the devices.

4. Conclusion

Plasma density is a key parameter that affects the exfoliation of graphite oxide. Applying a magnetic field in a direction perpendicular to the electrical field greatly enhances the dielectric barrier discharges. Subsequently, the threshold power for exfoliating the graphite oxide reduces from 120 W to 45 W with the magnetic field enhancement. The plasma exfoliated carbon materials possess graphene structures. N-doped graphene can be simultaneously achieved during the plasma exfoliation of the polyaniline modified graphite oxides. Flexible solid-state supercapacitors made of the plasma exfoliated graphene exhibit large specific capacitance of 45 mF/cm^2 at 0.2 A cm^{-2}, excellent capacitance retention of almost 100% after 1000 charge/discharge cycles at different current densities, and outstanding mechanical flexibility. The output potential can be simply increased by connecting multiple supercapacitors in series, which demonstrates the potential applications in flexible electronics. Magnetically enhanced plasma exfoliation of graphite oxide opens a cost-effective approach to manufacturing graphene for energy storage.

Acknowledgements

The authors acknowledge support from the National Science Foundation (Grant No. 1700785 and 1700787).

Appendix A. Supporting information

Supplementary data associated with this article can be found in the online version at doi:10.1016/j.ensm.2018.04.004.

References

[1] L. Yuan, X.-H. Lu, X. Xiao, T. Zhai, J. Dai, F. Zhang, B. Hu, X. Wang, L. Gong, J. Chen, ACS Nano 6 (2011) 656–661.
[2] X. Lu, M. Yu, G. Wang, Y. Tong, Y. Li, Energ. Environ. Sci. 7 (2014) 2160–2181.
[3] Y. Xu, Z. Lin, X. Huang, Y. Liu, Y. Huang, X. Duan, ACS Nano 7 (2013) 4042–4049.
[4] C. Meng, C. Liu, L. Chen, C. Hu, S. Fan, Nano Lett. 10 (2010) 4025–4031.
[5] M. Zhi, F. Yang, F. Meng, M. Li, A. Manivannan, N. Wu, A.C.S. Sustain, Chem. Eng. 2 (2014) 1592–1598.
[6] D. Yu, S. Zhai, W. Jiang, K. Goh, L. Wei, X. Chen, R. Jiang, Y. Chen, Adv. Mater. 27 (2015) 4895–4901.
[7] K. Wang, Q. Meng, Y. Zhang, Z. Wei, M. Miao, Adv. Mater. 25 (2013) 1494–1498.
[8] Y. Zeng, M. Yu, Y. Meng, P. Fang, X. Lu, Y. Tong, Adv. Energy Mater. (2016).
[9] A. Alabadi, S. Razzaque, Z. Dong, W. Wang, B. Tan, J. Power Sources 306 (2016) 241–247.
[10] Y. Shi, L. Pan, B. Liu, Y. Wang, Y. Cui, Z. Bao, G. Yu, J. Mater. Chem. A 2 (2014) 6086–6091.
[11] H. Zhou, H. Chen, S. Luo, G. Lu, W. Wei, Y. Kuang, J. Solid, State Electr. 9 (2005) 574–580.
[12] K. Wang, J. Huang, Z. Wei, J Phys. Chem. C 114 (2010) 8062–8067.
[13] K.S. Ryu, K.M. Kim, N.-G. Park, Y.J. Park, S.H. Chang, J. Power Sources 103 (2002) 305–309.
[14] H. Li, J. Wang, Q. Chu, Z. Wang, F. Zhang, S. Wang, J. Power Sources 190 (2009) 578–586.
[15] D. Li, J. Huang, R.B. Kaner, Acc. Chem. Res. 42 (2008) 135–145.
[16] F. Ran, Yt Tan, J. Liu, Lb Kong, Yc Luo, L. Kang, Polym. Adv. Technol. 23 (2012) 1297–1301.
[17] X. Cao, Y. Shi, W. Shi, G. Lu, X. Huang, Q. Yan, Q. Zhang, H. Zhang, Small 7 (2011) 3163–3168.
[18] Y. Zhu, S. Murali, W. Cai, X. Li, J.W. Suk, J.R. Potts, R.S. Ruoff, Adv. Mater. 22 (2010) 3906–3924.
[19] K.S. Kim, Y. Zhao, H. Jang, S.Y. Lee, J.M. Kim, K.S. Kim, J.-H. Ahn, P. Kim, J.-Y. Choi, B.H. Hong, Nature 457 (2009) 706–710.
[20] P.W. Sutter, J.-I. Flege, E.A. Sutter, Nat. Mater. 7 (2008) 406–411.
[21] S. Park, R.S. Ruoff, Nat. Nanotechnol. 4 (2009) 217–224.
[22] K.S. Novoselov, A.K. Geim, S.V. Morozov, D. Jiang, Y. Zhang, S.V. Dubonos, I.V. Grigorieva, A.A. Firsov, Science 306 (2004) 666–669.
[23] R. Liu, Y. Wang, D. Liu, Y. Zou, S. Wang, Adv. Mater. 29 (2017).
[24] S. Dou, C.L. Dong, Z. Hu, Y.C. Huang, Jl Chen, L. Tao, D. Yan, D. Chen, S. Shen, S. Chou, Adv. Funct. Mater. 27 (2017).
[25] Z. Liu, Z. Zhao, Y. Wang, S. Dou, D. Yan, D. Liu, Z. Xia, S. Wang, Adv. Mater. 29 (2017).
[26] Y. Wang, Y. Zhang, Z. Liu, C. Xie, S. Feng, D. Liu, M. Shao, S. Wang, Angew. Chem. 56 (2017) 5867–5871.
[27] K. Wang, M. Xu, Y. Gu, Z. Gu, J. Liu, Q.H. Fan, Nano Energy 31 (2017) 486–494.
[28] C.M. 5.3, Plasma Module User's Guide, COMSOL Inc., Stockholm, 2017.
[29] K. Tao, D. Mao, J. Hopwood, J. Appl. Phys. 91 (2002) 4040–4048.
[30] E.V. Barnat, P.A. Miller, A.M. Paterson, Plasma Sources Sci. Technol. 17 (2008) 045005.
[31] M.A. Lieberman, A.J. Lichtenberg, Principles of Plasma Discharges and Materials Processing, Wiley, New Jersey, 2005.
[32] R. Yang, J. Zheng, W. Li, J. Qu, X. Li, J. Phys. D: Appl. Phys. 44 (2011) 174015.
[33] S. Iordanova, I. Koleva, Spectrochim. Acta Part B 62 (2007) 344–356.
[34] S.A. Linnik, A.V. Gaydaychuk, Diam. Relat. Mater. 32 (2013) 43–47.
[35] D.L. Windsor, M.B. Denton, Appl. Spectrosc. 32 (1978) 366–371.
[36] C. Zhang, N. Mahmood, H. Yin, F. Liu, Y. Hou, Adv. Mater. 25 (2013) 4932–4937.
[37] A. Solonaru, M. Grigoras, Express Polym. Lett. 11 (2017) 127.
[38] D. Long, W. Li, L. Ling, J. Miyawaki, I. Mochida, S.-H. Yoon, Langmuir 26 (2010) 16096–16102.
[39] D. Geng, S. Yang, Y. Zhang, J. Yang, J. Liu, R. Li, T.-K. Sham, X. Sun, S. Ye, S. Knights, Appl. Surf. Sci. 257 (2011) 9193–9198.
[40] J. Yan, Z. Fan, T. Wei, W. Qian, M. Zhang, F. Wei, Carbon 48 (2010) 3825–3833.
[41] L. Wang, J. Kang, J.-D. Nam, J. Suhr, A.K. Prasad, S.G. Advani, ECS Electrochem. Lett. 4 (2015) F1–F4.
[42] W. Si, J. Zhou, S. Zhang, S. Li, W. Xing, S. Zhuo, Electrochim. Acta 107 (2013) 397–405.
[43] T. Zhu, J. Zhou, Z. Li, S. Li, W. Si, S. Zhuo, J. Mater. Chem. A 2 (2014) 12545–12551.
[44] Q. Hao, X. Xia, W. Lei, W. Wang, J. Qiu, Carbon 81 (2015) 552–563.
[45] C. Yang, L. Zhang, N. Hu, Z. Yang, Y. Su, S. Xu, M. Li, L. Yao, M. Hong, Y. Zhang, Chem. Eng. J. 309 (2017) 89–97.
[46] D.W. Wang, F. Li, L.C. Yin, X. Lu, Z.G. Chen, I.R. Gentle, G.Q.M. Lu, H.M. Cheng, Chem. -Eur. J. 18 (2012) 5345–5351.
[47] F. Su, C.K. Poh, J.S. Chen, G. Xu, D. Wang, Q. Li, J. Lin, X.W. Lou, Energ. Environ. Sci. 4 (2011) 717–724.
[48] X. Yang, D. Wu, X. Chen, R. Fu, J. Phys. Chem. C 114 (2010) 8581–8586.
[49] Z. Wang, Y. Han, Y. Zeng, Y. Qie, Y. Wang, D. Zheng, X. Lu, Y. Tong, J. Mater. Chem. A 4 (2016) 5828–5833.
[50] M. Biswal, A. Banerjee, M. Deo, S. Ogale, Energ. Environ. Sci. 6 (2013) 1249–1259.
[51] M.-J. Kwak, A. Ramadoss, K.-Y. Yoon, J. Park, P. Thiyagarajan, J.-H. Jang, ACS Sustain. Chem. Eng. 5 (2017) 6950–6957.
[52] A. Ramadoss, K.-Y. Yoon, M.-J. Kwak, S.-I. Kim, S.-T. Ryu, J.-H. Jang, J. Power Sources 337 (2017) 159–165.